




Room Acoustic Rendering Networks with Control of Scattering and Early Reflections

Matteo Scerbo , Lauri Savioja, *Senior member, IEEE* , Enzo De Sena, *Senior member, IEEE* 

Abstract—Room acoustic synthesis can be used in virtual reality (VR), augmented reality (AR) and gaming applications to enhance listeners’ sense of immersion, realism and externalisation. A common approach is to use geometrical acoustics (GA) models to compute impulse responses at interactive speed, and fast convolution methods to apply said responses in real time. Alternatively, delay-network-based models are capable of modeling certain aspects of room acoustics, but with a significantly lower computational cost. In order to bridge the gap between these classes of models, recent work introduced delay network designs that approximate Acoustic Radiance Transfer (ART), a GA model that simulates the transfer of acoustic energy between discrete surface patches in an environment. This paper presents two key extensions of such designs. The first extension involves a new physically-based and stability-preserving design of the feedback matrices, enabling more accurate control of scattering and, more in general, of late reverberation properties. The second extension allows an arbitrary number of early reflections to be modeled with high accuracy, meaning the network can be scaled at will between computational cost and early reverberation precision. The proposed extensions are compared to the baseline ART-approximating delay network as well as two reference GA models. The evaluation is based on objective measures of perceptually-relevant features, including frequency-dependent reverberation times, echo density build-up, and early decay time. Results show how the proposed extensions result in a significant improvement over the baseline model, especially for the case of non-convex geometries or the case of unevenly distributed wall absorption, both scenarios of broad practical interest.

Index Terms—Room acoustics modeling, Feedback Delay Networks, Room Acoustics Rendering Equation.

I. INTRODUCTION

THE field of room acoustics modeling is concerned with predicting the acoustical behaviour of environments. This finds application in a wide variety of areas, ranging from architecture and civil engineering – where designers need to account for speech intelligibility and noise levels in a space before it is constructed – to movies, video-games, and VR / AR applications – where reverberation can enhance listeners’ sense of realism [1], immersion [2], and externalization [3]. In many situations, it is desirable for the simulation to be performed in real-time, updating interactively while sound sources and receivers move in the virtual environment.

This work was supported by the Engineering and Physical Sciences Research Council under the SCalable Room Acoustics Modelling Grant EP/V002554/1.

Matteo Scerbo and Enzo De Sena are with the Institute of Sound Recording, University of Surrey, GU2 7XH Guildford, U.K. (e-mail: m.scerbo@surrey.ac.uk; e.desena@surrey.ac.uk).

Lauri Savioja is with the Department of Computer Science, Aalto University, 02150 Espoo, Finland (e-mail: lauri.savioja@aalto.fi).

Wave-based room acoustics models are based on the physical laws governing sound wave propagation, and can therefore account for all acoustic phenomena. This comes at the cost of considerable computational complexity, making such models unviable to run in real-time for broad-band signals. Geometrical acoustics (GA) models approximate the propagation of sound as being characterized by rays, as opposed to waves. This approximation cannot correctly capture phenomena such as room resonances and modal behaviour [4], a problem that can be addressed by considering hybrid wave-based/GA models [5]. Similar to other classes of models, GA ones do not result in “authentic” reproduction, in the sense that the difference between simulations and measurements of the same scene are clearly audible [6]. Crucially, however, they are capable of rendering acoustics in a manner that is sufficiently plausible, a more important criterion when rendering for video-games, music production and VR/AR [4], [6], [7].

Even with the fastest GA models, only a limited number of reflections can be simulated in real time with limited computational resources. The high reflection orders which characterize an environment’s perceived reverberation time lead to steadily increasing computational load. The predicted room impulse responses (RIRs) are most often applied to the source signal using convolution with both of the mentioned model classes. This yet increases the computational requirements – the computational cost of convolution scales with the duration of the RIR – and can introduce undesirable latency [8, Chap. 15].

A different way of applying reverberation to a signal is through the use of recursively connected delay lines. This characterizes the delay-based class of models, originating with the Schroeder reverberator [9], [10], with Feedback Delay Networks (FDNs) [11], [12] being the most widespread. These methods are more computationally efficient than any other, but do not intrinsically constitute physical models of an environment. Recent work [13]–[17] proposed room acoustics models that exploit the advantages of each method. These consist of delay-based structures while incorporating GA components in their design, thus providing fast modeling based on physical attributes of the space. Acoustic Rendering Networks (ARNs) [13] segment the room surface into patches, modeling the propagation of energy between them. FDN-ART [14] employs a small number of delay lines, based on the most prominent dimensions of the space. Scattering Delay Networks (SDNs) [15], [17] are designed around first-order reflection paths. Due to their relatively recent emergence, this class of models still suffers from some limitations with respect to convolution-based GA. They lack control of scattering

coefficients, an important acoustical parameter, and can only produce reliably accurate reflections for the first order.

Other works made joint use of GA and delay-based models, either by employing GA for early reflections and a delay-based model for late reverberation [18] or by partitioning the space to be modeled, computing responses for all partitions, and connecting the resulting “convolution blocks” with delay lines [19]. The focus of this paper is on methods that incorporate physically relevant information directly in a delay-based structure, to maximize physical accuracy and reliability while maintaining the efficiency of such models.

In this paper, we propose two key extensions of previous GA-oriented, delay-based models. Following work by Bai *et al.* [13], our extensions rely on the Room Acoustics Rendering Equation (RARE) – the analytical formulation underlying all GA models. First, we introduce two novel feedback matrix designs (“Sinkhorn-Knopp” design, “uniform” design), offering more flexible control of scattering for late reverberation. The second extension (high-order injection) enables the early response to be scaled between accuracy and computational efficiency, by selecting the number of reflection orders to be modeled with high fidelity outside of the recursive network. These extensions facilitate the modeling of environments with non-convex geometries or unevenly distributed wall absorption, as is often needed for practical applications.

Section II reviews the RARE and its discretization, the fundamental concepts of delay-network structures, and prior art delay-network-based models approximating the RARE. Section III details the construction and limitations of our proposed method, and Section IV illustrates its performance in several validation tests. Finally, Section VI presents concluding remarks and discusses future work.

II. BACKGROUND

This section will outline the fundamentals of radiance-based acoustic modeling and the Acoustic Radiance Transfer (ART) method. Then, it will illustrate the similarities and connections between ART and delay-network-based models. Finally, it will describe matrix design strategies employed in the prior art.

A. Geometrical Acoustics

As previously mentioned, GA models rely on acoustic rays to characterize sound propagation. The underlying mathematical model has its roots in geometrical optics [20, Chap 2]. When applied to acoustic energy propagating in rooms, said model takes the form of the Room Acoustics Rendering Equation (RARE) [21], which unfortunately cannot be solved analytically in the general case. In practice, GA methods, such as ray tracing or beam tracing, act as numerical solvers for this equation, with each model in the class being characterized by different approximations and/or discretizations.

Table I lists the notation¹ and terminology used in this paper for physical measures. The remainder of this subsection will describe radiance, the concept upon which the RARE is based on, followed by definitions of the RARE and ART.

¹This paper uses a notation similar but not identical to [21] and is meant to emphasise the links with delay-network-based room acoustic models.

TABLE I
Notation of the physical quantities used in this paper.

Notation	Units	Nomenclature
P	W	Power
$\Omega, d\omega$	sr	Solid angle
A, dA	m ²	Area
A_p, dA_p	m ²	Projected area
I	W m ⁻²	Sound intensity ^a
L	W sr ⁻¹ m ⁻²	Radiance
ρ	sr ⁻¹	BRDF
x, x', x''	m	Position vectors
v, n	N.A.	Direction vectors

^aIn the context of the RARE, sound intensity corresponds to the radiometric quantity called “irradiance” or “radiosity”. This is not to be confused with “radiant intensity”, a radiometric quantity measured in W sr⁻¹.

1) *Radiance*: Radiance, denoted by L , can be intuitively interpreted as energy traveling along the path of a ray – from a given point, in a given direction [21]. We will use the notation $v(x|x')$ for the directional vector based in x and pointed towards x' (see Fig. 1), therefore $L(x, v(x|x'), t)$ will denote the radiance emitted from point x in the direction of x' at time t . Formally, radiance is defined as the derivative of power over solid angle and projected area. For example, the power radiated from surface A_1 to surface A_2 at time t is [21]

$$P(A_1, A_2, t) = \iint_{A_2} \iint_{A_1} L(x, v(x|x'), t) d\omega_x(x') dA_{p_{x'}}(x), \quad (1)$$

where $dA_{p_{x'}}(x)$ is the differential area $dA(x)$ projected towards x' , and $d\omega_x(x')$ is the differential solid angle of the opening $dA(x')$ observed from x . Explicit expressions for these differential terms are reported in the Appendix.

2) *Room Acoustics Rendering Equation*: The RARE is a Fredholm integral equation of the second kind, characterizing the radiance between points on the entire reflective surface A of an environment. It is defined in [21], from which all the following remarks are drawn. In other words, given an environment defined by its boundary surface, the radiance reflected by each surface point is defined by the RARE as an integral sum of radiance contributions from all other surface points. This provides a recursive expression for the propagation of energy within the environment, over time. The RARE defines the radiance outgoing from the point x' in the direction of x'' at time t as

$$L(x', v(x'|x''), t) = \iint_A L(x, v(x|x'), t) * R(x, x', v(x'|x'')) dA(x) + L_0(x', v(x'|x''), t), \quad (2)$$

where $*$ denotes convolution (the R operator includes a time delay), and L_0 is the radiance originated² by the surface. The

²Notation in radiometry uses L_0 for the radiance being emanated by the surface – not reflected or transmitted. This is not relevant in acoustics, where it is common to separate energy sources from the reflecting boundary, and L_0 is instead considered to be the primary reflected radiance. See the Appendix for more details.

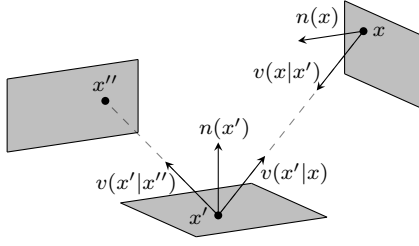


Fig. 1. Examples of directional vectors related to three boundary points.

term $R(x, x', v(x'|x''))$ is the so-called reflection kernel:

$$R(x, x', v(x'|x'')) = \rho(x'|v(x'|x), v(x'|x'')) \times G(x, x')V(x, x')D(x, x'), \quad (3)$$

where ρ models the scattering and energy losses (due to material absorption) at x' , G models the scaling of energy due to the distance and arrangement of $dA(x)$, $dA(x')$, V models the visibility between x , x' , and D models the propagation delay and air absorption between x , x' . See the Appendix for the explicit definitions of these terms, and a discussion of how sources and receivers are modeled in the RARE.

3) *Acoustic Radiance Transfer*: As previously mentioned, all GA methods constitute numerical solvers for the RARE. In particular, the Acoustic Radiance Transfer (ART) method [22] evaluates the integral in Eq. (2) by segmenting the entire reflecting surface A into N discrete patches A_1, A_2, \dots, A_N , and averaging the transferred radiance and reflection kernels over them. For example, the discretized surface radiance traveling from patch i to patch j is defined by integrating the continuous radiance over A_i and A_j . Time t is also discretized in samples, n . The discretized surface radiance at time sample n is defined by sampling the continuous radiance at time $t_n = n\Delta t$, where Δt is the discrete time step. Then, the discrete radiance \hat{L} can be defined with respect to the continuous radiance L as

$$\hat{L}_{i \rightarrow j}(n) = \iint_{A_j} \iint_{A_i} L(x, v(x|x'), n\Delta t) \frac{dA(x)}{A_i} \frac{dA(x')}{A_j}. \quad (4)$$

Note that $\iint_{A_i} f(x) \frac{dA(x)}{A_i}$ is the average value of f over A_i . The reflection kernel is expressed by a matrix $\hat{\mathbf{R}}$, with elements defined as

$$\hat{R}_{h \rightarrow i, i \rightarrow j} = \iint_{A_j} \iint_{A_i} \iint_{A_h} R(x, x', v(x'|x'')) \times dA(x) \frac{dA(x')}{A_i} \frac{dA(x'')}{A_j}, \quad (5)$$

which denotes the reflection kernel $h \rightarrow i \rightarrow j$, i.e. from patch h to patch j through patch i . The choice of subscript notation for $\hat{R}_{h \rightarrow i, i \rightarrow j}$ is meant to emphasise how the operator connects two paths, $h \rightarrow i$ and $i \rightarrow j$, which will be later modeled as delay lines. The indexing convention of $\hat{\mathbf{R}}$ is such that each row is associated with one of these paths and so is each column – the exact ordering is inconsequential. Note that the discretization of $\hat{\mathbf{R}}$ also involves a temporal discretization of the delay operators, left implied in (5).

The integral in Eq. (2), now discretized, is a sum:

$$\hat{L}_{i \rightarrow j}(n) = \sum_h^N \hat{L}_{h \rightarrow i}(n) \otimes \hat{R}_{h \rightarrow i, i \rightarrow j} + \hat{L}_{0, i \rightarrow j}(n), \quad (6)$$

where \otimes denotes discrete-time convolution, $\hat{L}_{0, i \rightarrow j}(n)$ is the discretized primary reflected radiance, and \sum_h^N is a summation over all N patches.

It should be noted that the convolution $\hat{L}(n) \otimes \hat{\mathbf{R}}$ in Eq. (6) results in temporal spreading, since the integration of the underlying delay operator $D(x, x')$ involves different delay values. In the simplest case, this operation is modeled as a scaling coefficient and a single (integer) delay, which is a reasonable approximation when the surface patches are small compared to the distance between them. Defining \mathbf{D} as the vector of time delays in $\hat{\mathbf{R}}$, and $\hat{\mathbf{S}}$ as the matrix of scaling coefficients of $\hat{\mathbf{R}}$, Eq. (6) takes the simplified form

$$\hat{L}_{i \rightarrow j}(n) = \sum_h^N \hat{L}_{h \rightarrow i}(n - D_{h \rightarrow i}) \hat{S}_{h \rightarrow i, i \rightarrow j} + \hat{L}_{0, i \rightarrow j}(n). \quad (7)$$

Note that, due to the energy-conserving property [23] of physically realistic bidirectional reflectance distribution functions (BRDFs) ρ , the matrix $\hat{\mathbf{S}}$ always satisfies the condition

$$\sum_h \hat{S}_{h \rightarrow i, i \rightarrow j} \leq 1 \quad \forall i, \forall j. \quad (8)$$

The methods proposed in Section III-A hinge on this property.

Finally, we define the *direct-incidence*, *injection*, and *detection* operators. The latter two are sometimes referred to as *initial tracing* and *final gathering*, respectively, and are typically computed using ray tracing. The injection operators, $\hat{s}_{i \rightarrow j}$, define the relationship between the source intensity and the primary reflected radiance:

$$\hat{L}_{0, i \rightarrow j}(n) = \hat{s}_{i \rightarrow j} I_s(n), \quad (9)$$

where $I_s(n)$ is the input sound intensity at a source point x_s .

The detection operators, $\hat{r}_{h \rightarrow i}$, define the relationship between the discretized radiance values $\hat{L}_{h \rightarrow i}(n)$ and the corresponding intensity contributions at a receiver point x_r , which make up the output sound intensity $I_r(n)$:

$$I_r(n) = \sum_i^N \sum_h^N \hat{r}_{h \rightarrow i} \hat{L}_{h \rightarrow i}(n) + \hat{b} I_s(n), \quad (10)$$

which also includes the direct-incidence operator, \hat{b} . Together, Eqs. (7), (9), and (10) form the complete ART acoustic model.

B. Delay-based modeling

Delay-based acoustic models, introduced in [9], [10], rely on inter-connected networks of delay lines to generate an output with an echo-rich structure. They circumvent the need for convolution with RIRs, which considerably reduces computational complexity under most conditions of practical significance. Among these models are Feedback Delay Network (FDN) structures [11], which revolve around a set of delay lines (d_i)

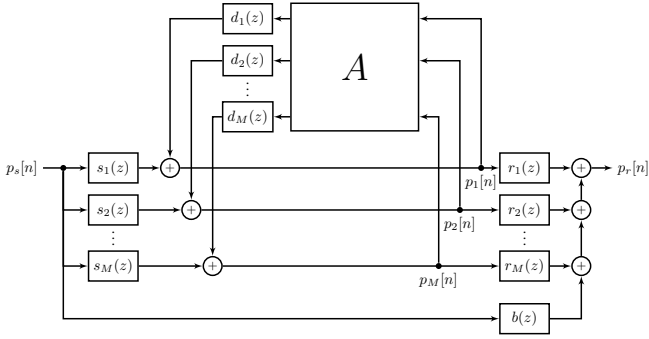


Fig. 2. Block diagram of the delay-based model structure used in this paper. Individual blocks can be either simple time delays and scaling coefficients, or more elaborate FIR filters. Note that this structure does not exactly match that of FDNs, because of the position of the delay operators in the loop and the presence of filters associated to each input and output.

and a feedback matrix (\mathbf{A}). In an FDN with M delay lines, the system output p_r is

$$p_r(n) = \sum_i^M r_i p_i(n) + b p_s(n), \quad (11)$$

$$p_i(n) = \sum_h^M A_{i,h} p_h(n - d_i) + s_i p_s(n - d_i), \quad (12)$$

where p_s is the system input, while s_i , r_i , and b are input and output weights (i.e. scalars, not operators). If $d_i = 1 \forall i$, Eq. (11), (12) correspond to the measurement and state equations of a state-space model, respectively. In other words, an FDN corresponds to a generalized version of a state-space model with non-unit delays [12].

An important aspect of FDN design is ensuring the system's stability, meaning that its output is bounded for any bounded input. All of the works described in the following employ so-called *unilossless* feedback matrices, \mathbf{A} , which guarantee stability for arbitrary (time-invariant) delay line lengths [24].

Most delay-based methods lack explicit physical parameters, and are instead calibrated based on the desired reverberation properties [4]. Recent work, discussed in the following, introduced geometrical acoustics concepts in the design of delay-based models. Note that the network structures of the discussed models, including the one proposed in this paper, are similar but not identical to the standard FDN structure. This is due in part to the presence of additional filters, and in part to the position of the delay operators in the feedback loop. In particular, the structure we employ (illustrated in Fig. 2) is designed to plainly display its links with ART.

1) *Acoustic Rendering Networks*: Acoustic Rendering Networks (ARNs) [13] leverage the similarity of the ART definition (Eq. (7), (10)) to the FDN structure (Eq. (11), (12)), designing a delay-based model using a surface discretization akin to ART. The main difference between the two is that the ART equations are intensity-based quantities (i.e. squared pressure), while delay-based models typically propagate pressure quantities. Scaling coefficients for air and surface materials are square-rooted to match this change in signal domain.

As a result, the feedback signals $p_{h \rightarrow i}$ traveling over the delay lines can be interpreted as root-radiance quantities:

$$p_{h \rightarrow i}(n) = \pm \sqrt{\hat{L}_{h \rightarrow i}(n)}. \quad (13)$$

Note that phase information, i.e. sign, is not preserved; this aspect is shared by all models which employ squared-pressure signals. Following the definition of ART, delay line lengths are based on the delay components \mathbf{D} , one for each path (pair of patches). The feedback matrix is only loosely based on $\hat{\mathbf{S}}$, and does not offer control of scattering coefficients – this will be discussed in more detail at the end of this section. Air and material absorption can be modeled by pairing each delay line with a filter, possibly frequency-dependent. The inputs of delay lines are weighted based on the injection operators (Eq. (9)), and the outputs are likewise weighted for detection (Eq. (10)).

2) *FDN-ART*: The FDN-ART method [14] also starts from a surface discretization, but rather than trying to match the delay-based structure of ART, it generates a small number of delay lines based on the most commonly occurring values in \mathbf{D} . The process aims to detect the environment's salient modes, by selecting delay line lengths related to the major resonance frequencies. The details of the feedback matrix design are not relevant in the context of this paper, as the resulting matrices do not preserve spatial information (lines don't correspond to physical paths). As in ARN, wall and air absorption are modeled by filters associated to each delay line.

The network structure is designed in such a way that the feedback loop only generates reflections from the second reflection order onwards, while first order reflections are modeled by additional delay lines bypassing the loop. For this reason, first order reflections may be modeled by any GA method of choice, depending on the desired accuracy of the early impulse response.

C. ARN matrix design and sparseness of ART matrix

Before discussing the design of ARN recursion matrices, \mathbf{A} , it will be useful to illustrate some properties of ART recursion matrices, $\hat{\mathbf{S}}$. Aside from providing insight on the functioning and design of \mathbf{A} , this will show how the cost of operations on these matrices can be reduced from N^4 to N^3 or less.

We will examine the structure of $\hat{\mathbf{S}}$ with the help of an example matrix (shown in Fig. 3) related to a cuboid room of size $2 \text{ m} \times 2 \text{ m} \times 6 \text{ m}$, reflection coefficient 0.9, and scattering coefficient 0.25. The room is divided in 6 surface patches, one for each wall. Note that this is an extremely coarse discretization, for illustrative purposes; much smaller patches are generally used in ART. The elements of $\hat{\mathbf{S}}$ contoured by red dashed lines in Fig. 3a form the sub-matrix $\hat{\mathbf{S}}_1$ shown in Fig. 3b. The contoured rows are those related to lines which end at patch 1 (the floor), and the contoured columns are those related to lines which start from the same patch. Each block $\hat{\mathbf{S}}_i$ defined this way characterizes the scattering behaviour of the corresponding patch i . With this in mind, the reason why $\hat{\mathbf{S}}$ is so highly sparse (most elements are 0) is that any line terminating at a given patch i only provides contributions to the lines which depart from the same patch, i.e.

$$\hat{S}_{h \rightarrow i, j \rightarrow k} = 0 \quad \forall i \neq j, \quad (14)$$

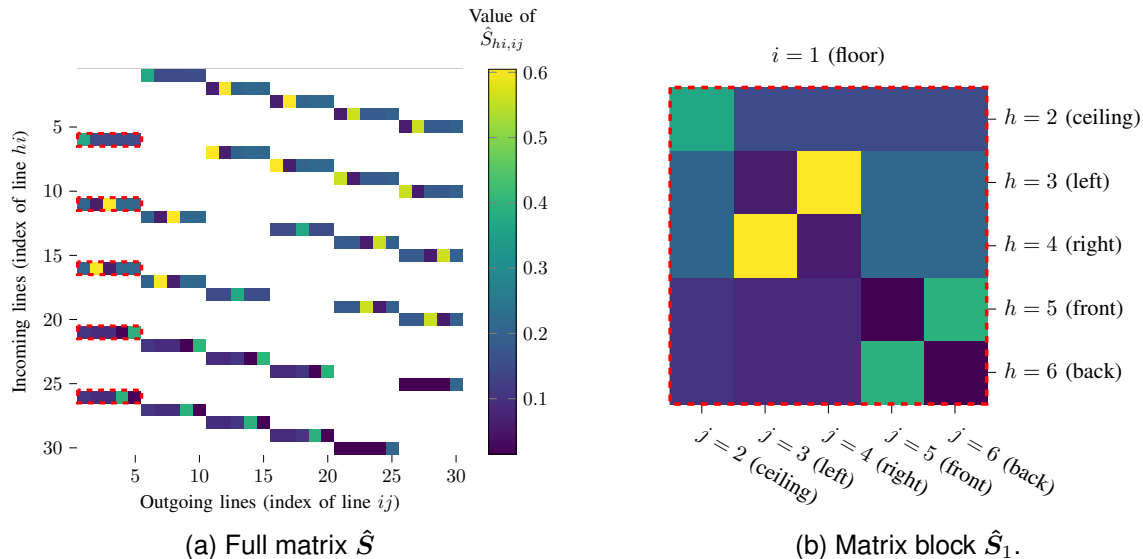


Fig. 3. \hat{S} matrix for a “hallway” room of size $2\text{ m} \times 2\text{ m} \times 6\text{ m}$, reflection coefficient 0.9, and scattering coefficient 0.25. Note that values of 0 are drawn in white. The elements contoured by red dashed lines in 3a make up the block \hat{S}_1 shown in 3b, where 1 is the floor patch index.

because a patch can only scatter energy to and from the paths connected to it. This observation leads to a considerable reduction in the computational cost of designing and employing matrices based on \hat{S} , as we will discuss in the following.

It is possible for even more elements of \hat{S} to be 0. If there is no direct visibility between a pair of patches h, i , two rows and two columns will be entirely 0 – those corresponding to the two paths $h \rightarrow i, i \rightarrow h$, which relate to one row and one column each. Of course, paths without visibility carry no energy in either direction, and the redundant delay lines should be removed from the network along with the corresponding matrix entries. The same applies to paths connecting each patch to itself, or to any other patch located on the same flat surface. In Fig. 3, self-interaction paths have already been removed.

With these properties in mind, we can now clearly see how the complexity of matrix operations can be reduced from N^4 to N^3 or less. With N surface patches, there are up to N^2 delay lines (patch pairs), therefore up to N^4 elements in \hat{S} . Due to Eq. (14), nonzero elements are N^3 in total (N blocks of size $N \times N$ each). Lack of visibility may further reduce the size of each block. Awareness of the null elements does not only reduce the computational complexity of running the recursive system, but also the complexity of the matrix design.

The original ARN [13] makes use of a permuted Householder matrix for each block A_i of the feedback matrix A . The first step in this design is the evaluation of a permutation matrix, P_i . The evaluation, detailed in the next paragraph, is such that the nonzero elements of P_i correspond to pairs of delay lines which form specular reflections. Then, in each block A_i , the elements chosen as “specular” are set to $(2 - M_i)/M_i$, where M_i is the size of the block A_i , and the remaining elements³ are set to $2/M_i$. As a result, A_i is

³Note that paths without visibility were removed: all elements in each block A_i correspond to patches which are visible from patch i .

a permuted Householder matrix, and the elements related to specular reflections carry more energy than others.

It should be noted that the creation of the “specular” permutation matrix P_i is not trivial. Bai *et al.* [13] select for each column in \hat{S} the path which receives the most specularly reflected energy. However, there are several instances where this strategy does not yield an actual permutation matrix, and it is unclear how these cases are handled in [13]. An example of a problematic situation is illustrated in Fig. 4. In the example, two different columns (corresponding to lines $i \rightarrow j$ and $i \rightarrow k$) would select the same row (corresponding to line $h \rightarrow i$) as the direction of most specularly reflected energy. With more than one non-zero element on a single row, the result is not a permutation matrix. This is, in fact, the case for all but the most trivial geometry discretizations.

The strategy used in the remainder of this paper to obtain such permutation matrices consists of iteratively selecting the maximum value in \hat{S} , setting the corresponding element to 1 in the matrix, and ignoring the selected row/column pair in subsequent iterations. The resulting matrix is guaranteed to be a permutation matrix, and the conflicts illustrated above are resolved by prioritizing higher energy transfers.

In the next section, we will discuss the limitations of the permuted Householder matrix design, and propose two methods to overcome them.

III. PROPOSED MODEL

The extensions proposed in this paper are based on the ARN interpretation of feedback signals as root-radiance quantities (see Eq. (13)). This interpretation can be leveraged to obtain higher accuracy and flexibility in the recursive component of reverberation, as well as in the early reflections. The first extension, presented in Section III-A, is focused on the design of the feedback matrix A , with the objective of obtaining more accurate reverberation times and preservation of spatial information (i.e. energy flowing over each path in space, at

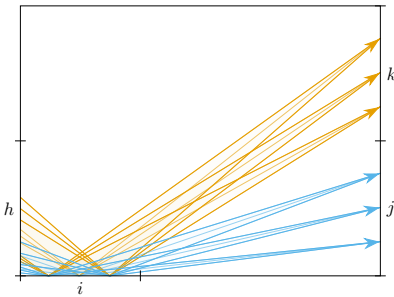


Fig. 4. A possible situation where “naive” pairing of specular paths fails to produce a permutation matrix. Given patch i as a reflector, it is clear that the incoming direction $h \rightarrow i$ holds the most specularly reflected energy for both outgoing directions $i \rightarrow j$, $i \rightarrow k$. For visual clarity, very few sample points are shown on the areas A_i , A_j , A_k ; evaluating Eq. (5) with fine discretization does not prevent the effect.

each point in time). The second extension, presented in Section III-B, is focused on the design of the input operators s_{ij} , with the objective of obtaining more accurate early reflections. Section III-C presents the design of the remaining system components (recursion, detection, and bypassing operators).

A. Physically-driven feedback matrix designs

The Householder matrix design employed in [13] has two drawbacks. The first is that it offers no control of scattering coefficients. Instead, the ratio of specular-to-diffuse energy is controlled entirely by the size of matrix blocks, M_i , which, in turn, is set by the surface discretization resolution. The second drawback, also related to the block size M_i , is that the Householder matrices tend towards simple identity matrices as M_i increases. Note that high surface discretization resolution is required for good modeling accuracy of ART: attempting to increase the spatial resolution of the model induces the aforementioned artefacts. This has adverse effects on the reverberation times and echo density produced by the ARN, as will be shown in Section IV.

The objective of the extensions proposed in this section is to design the feedback matrix \mathbf{A} such that it achieves a closer match to the ART matrix $\hat{\mathbf{S}}$, all the while preserving stability. To enable the use of arbitrary scattering coefficients (and in theory, arbitrary BRDFs), we propose adapting the *closest sign-agnostic matrix* optimization process introduced by Schlecht and Habets [25]. The process is intended to generate the unilossless feedback matrix \mathbf{A} which most closely matches a given target matrix $\tilde{\mathbf{A}}$, with a focus on the absolute values of entries, which govern energy distribution. The sign-agnostic optimization is restricted to target matrices such that their Hadamard (i.e. element-wise) square $\tilde{\mathbf{A}} \circ \tilde{\mathbf{A}}$ is doubly-stochastic (i.e. each row sums to 1, as do the columns)⁴. Unfortunately, although the columns of $\hat{\mathbf{S}}$ sum to 1 (see Eq. (8)), the same is not necessarily true of its rows.

In order to apply the closest sign-agnostic optimization here, it is necessary to first find the closest doubly-stochastic matrix

⁴Note that if there exists a non-singular diagonal matrix \mathbf{E} such that $\mathbf{B} = \mathbf{E}\tilde{\mathbf{A}}\mathbf{E}^{-1}$ is doubly-stochastic, using \mathbf{B} in place of $\tilde{\mathbf{A}}$ and compensating for \mathbf{E} in the input-output parameters results in an equivalent system (see Theorem 3 in [24]).

to $\hat{\mathbf{S}}$. Before proposing two strategies for this problem, it is useful to note that because of the property in Eq. (14), $\hat{\mathbf{S}}$ is doubly stochastic if and only if each block $\hat{\mathbf{S}}_i$ is doubly stochastic. This is because all nonzero elements lying on a given row hi in $\hat{\mathbf{S}}$ define one row of one block $\hat{\mathbf{S}}_i$, and all nonzero elements lying on a given column ij define one column of one block $\hat{\mathbf{S}}_i$ (this can be verified visually in Fig. 3a). As a result, either one of the proposed approaches can be applied to individual blocks $\hat{\mathbf{S}}_i$ to greatly reduce operations.

Two separate design strategies are presented here and compared in Section IV. One strategy results in a higher accuracy but can fail under certain conditions, while the other is more approximate but prevents such failure conditions.

1) *Sinkhorn-Knopp matrix design*: The first approach uses the Sinkhorn-Knopp algorithm [26], which provides the closest doubly-stochastic matrix to a target. More precisely, given the target $\hat{\mathbf{S}}_i$, Sinkhorn-Knopp provides the diagonal matrices $\mathbf{E}_1, \mathbf{E}_2$ such that $\tilde{\mathbf{A}}_i \circ \tilde{\mathbf{A}}_i = \mathbf{E}_1 \hat{\mathbf{S}}_i \mathbf{E}_2$ is doubly-stochastic.

A necessary and sufficient condition for the Sinkhorn-Knopp algorithm to converge is that the target matrix has total support [26], [27]. There are some cases where this is not the case for $\hat{\mathbf{S}}_i$, and Sinkhorn-Knopp is not applicable. For example, if there is no diffuse component to the BRDF of patch i , energy traversing a path hi will be reflected towards a few – but not all – patches visible from i . As a result, different rows in $\hat{\mathbf{S}}_i$ may have different numbers of nonzero elements, and the block may not have total support, leading to divergence (elements in $\mathbf{E}_1, \mathbf{E}_2$ tend to infinity).

Note how this strategy allows modeling of arbitrary scattering coefficients as well as arbitrary BRDFs.

2) *Uniform matrix design*: The second approach uses a simplified scattering model. Similarly to the Householder matrices used in [13], the starting point is a permutation matrix \mathbf{P}_i correlating the pairs of paths that carry the most specular energy. Then, for each block $\hat{\mathbf{S}}_i$, the nonzero elements of the permutation matrix are set to $(1 - \sigma_i)$, where σ_i is the scattering coefficient of patch i . The remaining elements are set to $(\sigma_i / (M_i - 1))$, where M_i is the size of $\hat{\mathbf{S}}_i$. With this configuration, the ratio of specular to diffuse energy is controlled by the scattering coefficient – and the resulting matrix is doubly-stochastic, so the sign-agnostic optimization can be applied directly.

Note that this strategy allows for arbitrary scattering coefficients but not arbitrary BRDFs. Also, note that neither this matrix design nor the Householder matrix design proposed in [13] are equivalent to ideally diffuse scattering, since they redirect equal amounts of energy towards each patch regardless of the size, distance, and relative orientation of patches.

B. High-order injection

The second proposed extension is related to the injection operators, with the objective of enabling finer control of early reflections. The injection operators are marked by s_{ij} in Fig. 2. Note that we are here abusing notation, with the subscript in the figure indicating the delay line index, while the ones used in the text indicate the path between two patches.

As explained in Section II, in [13] the “initial tracing” step of ART is used to evaluate the direct incidence radiance from

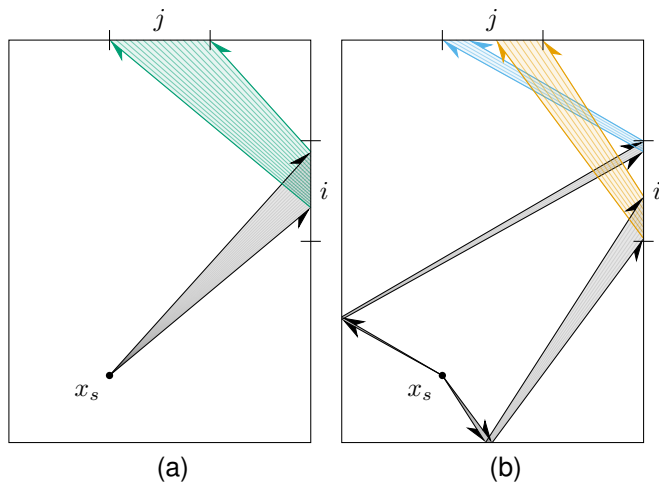


Fig. 5. Evaluation of $\hat{L}_{0,ij}(n)$ (5a) and $\hat{L}_{1,ij}(n)$ (5b). The reflections shown here are strictly specular for visual clarity, while evaluation of network parameters may include scattering.

the source, while in [14] it is used to evaluate the primary reflected radiance for each discrete path. The former ensures accurate rendering only of the direct component, the latter only of the direct component and first-order reflections.

In our model, the injection operators are designed to inject radiance of order K into the system. That is to say, rather than basing their design on direct incidence radiance (see Eq. 9), the radiance is reflected K times before being assigned to delay lines. Orders smaller or equal to K are modeled via a filter (marked as b in Fig. 2) that bypasses the recursive part of the network.

A similar approach is commonly used in hybrid models involving the image model and FDNs [4]. SDNs have been recently extended in a similar fashion [28], [29], but are still limited to rectangular geometries.

The injection radiance may be evaluated using ray-tracing, as is common practice for ART and ARN. Unlike ART and ARN, however, the process we propose is carried out over reflection orders larger than one. During the tracing process, each ray keeps memory of intersected patch indices, halting at the $(K+2)$ th intersection. Then, evaluation of order K average radiance $\hat{L}_{K,ij}(n)$ is based on the rays which hit patch i at their $(K+1)$ th reflection and patch j at the $(K+2)$ th. The example in Fig. 5 shows the relevant ray bundles for delay line ij , with injection order $K=0$ (5a) or $K=1$ (5b).

Two injector designs are considered here. The first design is a simple combination of a delay line and a scaling coefficient, as used in the original ARN [13]. The length of the delay line is calculated as the average travel time of the relevant rays, and the scaling coefficient is calculated as the square root of their average radiance.

A second approach is proposed here to enhance the modeled echo density, where the injectors operators are modeled using FIR filters taking into account the temporal spreading of the ray bundle. This is inspired by the approach used in [22] for recursive temporal spreading (note that we only add dispersion to the injection/detection operators, and not to recursive operators). The gathered rays are first used to produce an energy

impulse response [8, Chap. 11]. The energy response is then divided by the total gathered radiance to obtain the required average, and finally its square root is used to modulate a noise signal, as is common practice in models based on squared pressure [30]. In the example of Fig. 5b, an injector including temporal spreading would correctly capture the two reflection paths as separate impulses, while a “weighted delay” injector would merge them into one.

Both of these methods enable the modeling of directional sources, by incorporating them into the ray tracing.

C. Other parameters

In the following, we discuss the design of the remaining operators – blocks r_{ij} , d_{ij} , b in Fig. 2.

1) *Detectors*: The detection operators r_{ij} are evaluated similarly to the injection operators, by performing ray tracing, this time without performing any reflections. The key difference is that the radiance of each bundle is not averaged.

Like the input operators, these can either be designed as simple scaled delays for simplicity, or include temporal spreading for richer echo density. Receiver directional patterns are just as easily incorporated in the evaluation. In particular, note that each detection operator r_{ij} is related to a surface patch j , at a known distance and direction relative to the listener. As such, the patches can be treated as individual audio objects for spatialization / binaural reproduction. If so desired, the detection and bypass operators can include filters – e.g. head-related transfer functions (HRTFs) – to carry out the spatial panning. Simulation of microphone arrays is also possible, by modeling each pick-up point as a separate “listener object”, and creating a separate set of detection operators for each one.

Since the output of injection operator s_{ij} corresponds to the signal reaching patch j from the direction of i , and the detection operator r_{ij} relates that same quantity to the signal reaching the receiver from patch j , the two components in series produce a reflection of order $K+1$ (s_{ij} performs $K+1$ reflections, r_{ij} none).

2) *Delays*: The length of delay lines are based on the discrete delays D . In addition to the time delay, the d_{ij} operators apply wall and air absorption, both of which may be frequency dependent. Incorporating wall and air absorption in d_{ij} is preferred over incorporating them in A to keep A unilossless. This is easily achieved by use of normalized BRDFs and random-incidence absorption coefficients, as is common practice in GA.

3) *Bypass*: The final component is the filter b , bypassing the recursive network. It models reflections of orders $\leq K$, including the line-of-sight component. The simulations in the remainder of the paper employed Image Source Method (ISM) to better model the impulsive nature of early reflections, but other methods can be used too. For example, the operator may be evaluated during the same ray-tracing step as the injection operators, in which case it does not increase the computational complexity.

IV. EVALUATION

The proposed models were validated against two well-established GA models (Ray Tracing Method (RTM) and Im-

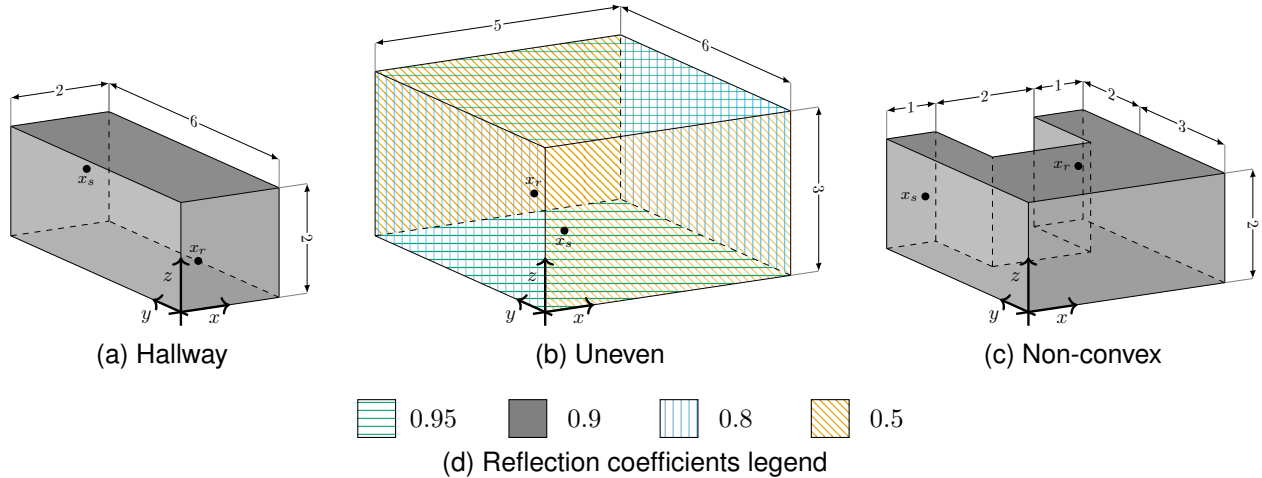


Fig. 6. Geometry of the rooms presented in this paper, detailed in Table II.

age Source Method (ISM)), as well as real measurements. The evaluation alongside GA simulations was carried out to ensure a fair comparison, by considering simple scenarios with one defining characteristic (e.g. unevenly distributed absorption or non-convex geometry, not both). This granularity makes it possible to gauge each extension’s contribution in relation to different properties of the scene. The evaluation alongside real measurements acts as a more thorough validation of the method, in a more complex scenario with frequency-dependent and unevenly distributed absorption coefficients. In both cases, comparisons were based on objective metrics, described in the following section.

Since our method is based on GA, it inherits the limitations dictated by the acoustic ray approximation. For this reason, it was deemed unnecessary to perform comparisons with wave-based simulations and/or examine the low-frequency performance in detail.

A. Objective measures

The reverberation time of each response was evaluated using octave-band T_{30} values. The performance in terms of the early response was quantified using early decay time (EDT) and normalized echo density (NED). These quantities are defined as follows. early decay times and T_{30} are based on energy decay curves (EDCs), a measure of the energy remaining in a RIR over time [31, Sec. 3.8], defined as

$$\text{EDC}(n) = \frac{\sum_{i=n}^{\infty} h^2(i)}{\sum_{i=0}^{\infty} h^2(i)}, \quad (15)$$

where $h(n)$ is a RIR. These can be evaluated for separate frequency bands as well as for the full, broadband RIR. The T_{60} value, measured in seconds, is defined as the moment the EDC passes -60 dB; T_{30} shares that definition, but is computed based on a linear regression of the EDC in the range -5 dB to -35 dB. early decay time is defined as the moment the EDC passes -10 dB.

The normalized echo density (NED) is a measure devised to estimate the perceived sense of sound diffusion in a space [32]. It is defined, for a given time window of the RIR, as the ratio

between the number of samples lying more than a standard deviation away from the mean and that which is expected for Gaussian noise.

B. Simulation comparisons

The GA models used as references are CATT-Acoustics [33] (a state-of-the-art RTM model) and PyRoomAcoustics [34] (an ISM model). The ISM does not model scattering and is only shown as a reference for a single scenario with low scattering.

Simulation examples included three feedback matrix designs (Householder, Sinkhorn-Knopp, uniform), both injection operator designs (with or without time spreading), several injection orders K , and several surface discretization levels. Results marked as “ARN baseline” use Householder matrix designs and injection operators with $K = 1$ and no time spreading, combining the advantages of ARN [13] and FDN-ART [14].

Reflection kernels were evaluated based on the common “pseudospecular” BRDF [21], performing the integral in Eq. (5) by sampling each reflector at 0.5m intervals and performing ray-tracing Monte Carlo integration from each sample point. Injection and detection operators were evaluated using ray-tracing as previously described, while the bypass filter was evaluated separately using ISM.

Simulated environments included two rectangular rooms and one non-convex room, all of which were tested for different source-receiver configurations, scattering coefficients, and wall absorption coefficients, including scenarios with unevenly-distributed absorption. All simulations used the same air absorption parameters (50% humidity, 20°C) and omnidirectional source and receiver. All responses were processed with a 20 Hz high-pass filter. Note that all reported octave-band plots start from 125 Hz center frequency, as that is the lowest frequency band modeled by CATT-Acoustics.

Only some salient examples are reported here, while all setups and responses are available online [35]. The environments presented in the following are detailed in Table II, and illustrated in Fig. 6.

Note that the employed wall absorption coefficients are frequency-independent, and the high-frequency roll-off ob-

TABLE II

Parameters used for the room simulations presented in this paper. For the “non-convex” room, the size reported here is that of the bounding box.

Descriptor		Hallway	Non-convex	Uneven
Size	x	2 m	4 m	5 m
	y	6 m	5 m	6 m
	z	2 m	2 m	3 m
Source pos.	x	1.2 m	0.5 m	1.2 m
	y	5.4 m	4.5 m	1.4 m
	z	1.2 m	1.0 m	1.0 m
Mic pos.	x	0.7 m	3.5 m	0.7 m
	y	0.6 m	4.3 m	1.6 m
	z	0.7 m	1.2 m	1.7 m
Reflection coeff.		0.9	0.9	0.95, 0.8, 0.5
Scattering coeff.		0.25	0.25	0.05

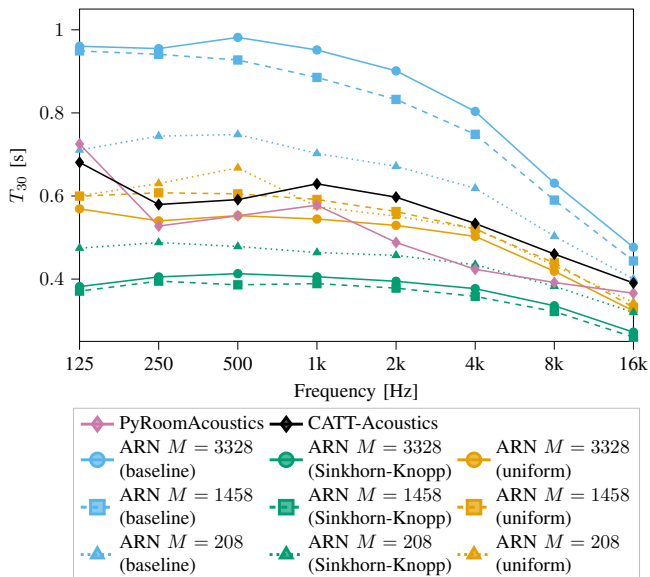


Fig. 7. Octave-band T_{30} values for the “uneven” room. All ARNs use basic injectors with $K = 1$ and no time dispersion.

served in the results is entirely due to air absorption. Frequency-dependent wall absorption coefficients can easily be employed as part of the delay operators as discussed in the previous section, but were not included here for simplicity.

1) *Reverberation time*: Fig. 7 shows the octave-band T_{30} values in the room with uneven absorption. The first observation to be made here relates to the baseline ARN model, which shows an over-estimation of the T_{30} at all frequencies. Crucially, the overestimation worsens with increased spatial discretization. Matrix sizes of $M = 208$ correspond to a discretization with $N = 16$ patches, $M = 1458$ to $N = 42$ patches, and $M = 3328$ to $N = 64$ patches. This is due to the fact that in the baseline ARN, the scattering matrix is given by a Householder transformation whereby the specular-to-diffuse energy ratio depends on the matrix size. This is clearly problematic, since it gives rise to a trade-off between spatial accuracy and T_{30} accuracy.

The proposed “uniform” design, on the other hand, produces reliably accurate reverberation times, with minimal variation

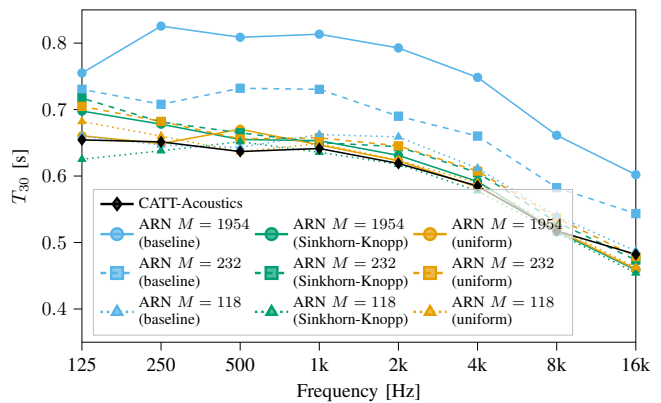


Fig. 8. Octave-band T_{30} values for the “non-convex” room. All ARNs use basic injectors with $K = 1$ and no time dispersion.

when the matrix sizes change. The proposed “Sinkhorn-Knopp” design results in an underestimation of T_{30} values, but is still closer to CATT-Acoustics compared to the baseline.

The large differences in T_{30} obtained with different feedback matrix designs suggest that, in environments with uneven absorption such as the one shown, scattering plays an important role in reverberation times. This is supported by results not presented here for space reasons, which show that CATT-Acoustics produces different T_{30} values for different scattering coefficients. Said difference is most pronounced in the uneven room, but also appears in the non-convex one.

Householder matrices can also lead to incorrect T_{30} values in some uniform absorption cases, such as the non-convex room. Fig. 8 shows the T_{30} results for said room. Like for the uneven-absorption room, CATT-Acoustics suggest an influence of the scattering coefficients on reverberation times for the non-convex room, although it was less pronounced in this case. In this instance, both of the proposed designs perform well, matching the reference (CATT-Acoustics) very closely regardless of the discretization level. In this case, $M = 118$ corresponds to a discretization with $N = 14$ patches, $M = 232$ to $N = 19$ patches, and $M = 1954$ to $N = 58$ patches.

In rectangular rooms with uniform absorption coefficients, such as the “hallway” room, all ARNs – including the baseline – generally produce correct T_{30} values. Such environments have been tested in previous works employing Householder matrices [13], [15], [28], [29].

2) *Early decay time*: Householder matrices with a large size can also cause inaccurate modeling of early decay time (EDT). More specifically, they can result in an abrupt drop in energy between early and late reflections, an effect previously observed in [15], [28], [36], [37], regardless of the room shape and the absorption coefficients. Both of the proposed matrix designs prevent this effect. Fig. 9 shows examples of octave-band EDT values for different matrix designs and injector designs. Householder matrices (shown only for the “baseline”) lead to excessive EDT for all frequency bands above 500 Hz. The “uniform” matrix design leads to more accurate values regardless of the employed injector design; “Sinkhorn-Knopp” design results (not shown in Fig. 9) were

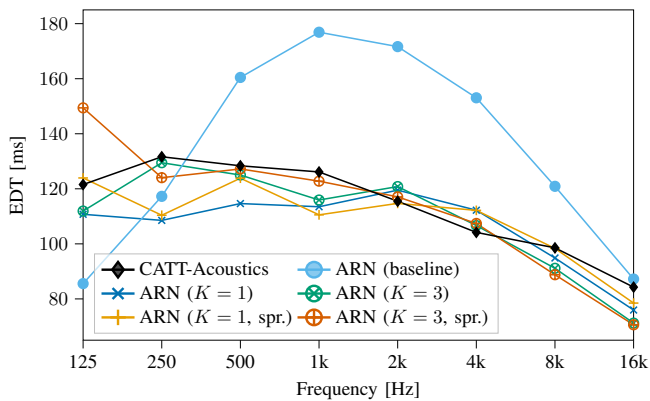


Fig. 9. Octave-band EDT values for the “non-convex” room. The “baseline” ARN uses a Householder matrix as usual, while the proposed ones use the uniform matrix design. The matrix size for all ARNs is $M = 1954$, corresponding to $N = 58$ patches.

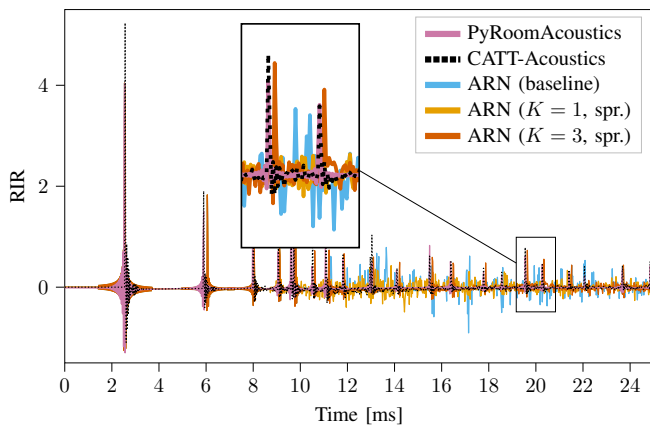


Fig. 10. room impulse response for the “uneven” room comparing the injection operators with and without temporal spreading, and for different injection orders, K . The “baseline” ARN uses a Householder matrix as usual, while the proposed ones use the uniform matrix design. The matrix size for all ARNs is $M = 3328$, corresponding to $N = 64$ patches.

similarly accurate. With either of the proposed matrix designs, a slight improvement in accuracy can be seen when the injection order is raised from $K = 1$ to $K = 3$. Note that introducing temporal spreading in the injector design has minimal effects on the EDT.

3) *Early reflections*: Increasing the injection order K improves the accuracy of prominent early reflections. This can be seen in the RIRs in Fig. 10. The inset plot highlights a part of the RIR where the proposed method with $K = 3$ produces exact reflections while the baseline and proposed method with $K = 1$ do not.

Fig. 11 further illustrates the increase in accuracy of the early response, in the form of EDCs. The illustrated “hallway” room is a rectangular room with uniform absorption coefficients, a scenario where the baseline produces correct reverberation times. This was chosen to ensure a fair comparison, since the different decay in other rooms affects the early portion of the EDC as well. Moreover, the presented case is one with very coarse surface discretization, for reasons

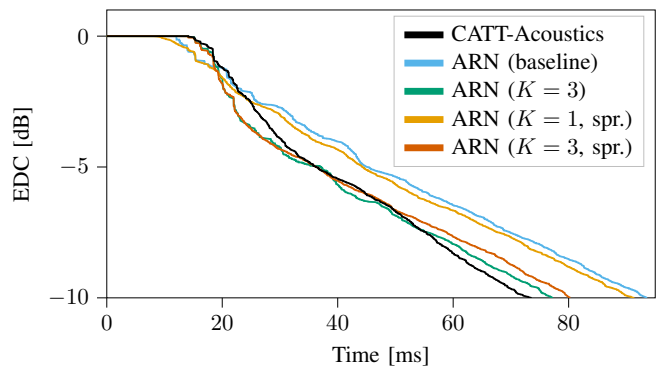


Fig. 11. Early section of the energy decay curve for the “hallway” room. Comparison of injectors with or without temporal spreading, K marks the injection order. All ARNs use a Householder matrix. The matrix size for all ARNs is $M = 30$, corresponding to $N = 6$ patches.

explained in the next subsection.

Fig. 11 shows how increasing the injection order K improves the profile of the early decay, resulting in improved EDT prediction (as in Fig. 9). It can be observed that, as anticipated by the EDTs, the presence of temporal spreading has negligible effect on the late energy decay.

Fig. 11 also shows certain artefacts resulting from the coarse discretization of the boundary. For instance, in the $K = 1$ case, the RIR onset begins even earlier than the line-of-sight component. This is due to the fact that early signals traveling through the delay lines can find much shorter paths than would be expected. This is particularly evident in cases like the one shown here, where the source and receiver are positioned at opposite ends of the elongated space and lengthy surfaces are modeled by individual patches. Increasing K does not remove these excessively short paths from the system, but it delays the onset of this type of artefacts.

It should be noted that increasing the spatial discretization reduces these artefacts, but at a significant computational cost. The proposed higher-order injection method, on the other hand, allows accurate control of the early reflections with only a small impact on the computational complexity.

4) *Normalized Echo density*: Fig. 12 shows the time evolution of NED produced with the same simulation setup as Fig. 11. Two effects can be observed for the case $K = 3$ with no temporal spreading. First, the very early echo density is closer than the baseline to CATT-Acoustics, thanks to the bypass filter producing correct early reflections. Then, after about 15ms, the density decreases below the baseline: this is due to the fact that with large surface patches, groups of high-order reflections get “bundled” together (e.g. see Fig. 5b). Using $K = 3$ injectors with temporal spreading resolves this issue, because multiple reflections in one injector lead to an increase in echo density, getting closer to CATT-Acoustics.

It should be noted, however, that temporal spreading can cause an excessive echo density when used with injectors of low order. For instance, Fig. 12 shows the $K = 1$ case with temporal spreading, which results in a very high echo density being produced too soon. This is due to the fact that with very large surface patches, the recursive delay lines lead to

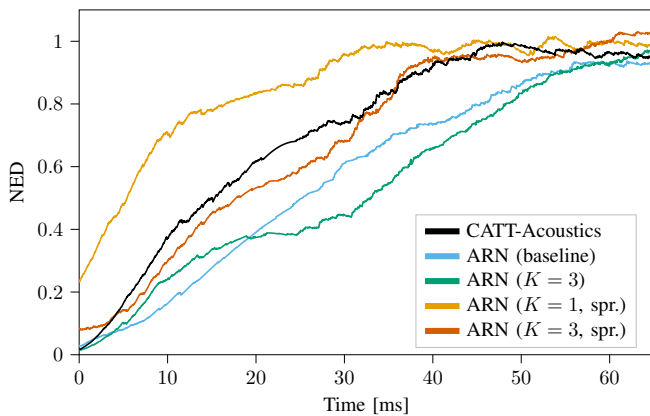


Fig. 12. NED for the “hallway” room. Comparison of injectors with or without temporal spreading, K marks the injection order. NED window length 25 ms. All ARNs use a Householder matrix. The matrix size for all ARNs is $M = 30$, corresponding to $N = 6$ patches.

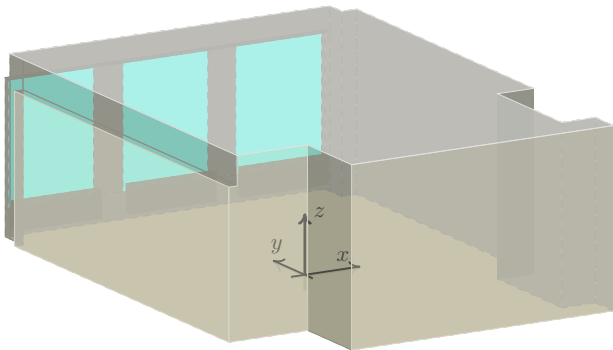


Fig. 13. The simplified model of scene CR2 [38] used for validation. Note that some details of the original model were removed (ceiling lights, small protrusions on right wall).

premature diffusion, as discussed in the previous sub-section. When combined with the “noisy” temporal spreading design, this makes the echo density rise excessively fast. A higher injection order, like $K = 3$, prevents this by design.

C. Measurement comparisons

The CR2 scene from the Benchmark for Room Acoustical Simulation (BRAS) dataset [38] was employed for the comparison against ground-truth measurements. The model’s geometry was slightly simplified (as shown in Fig. 13) in order to reduce the number of polygons with small area. The parameters provided in the dataset were used to model frequency-dependent air and wall⁵ absorption, however the scattering was modeled with frequency-independent coefficients, since the unilossless optimization of polynomial matrices is still an open problem. Each material was modeled using the provided scattering coefficient at 4 kHz.

The measurements made using the dodecahedral speaker were chosen as reference, and the speaker was modeled as a single point source at the position of the high-frequency unit. All loudspeaker and microphone positions were tested. The

⁵The “fitted” absorption coefficients were employed, see [38] for details.

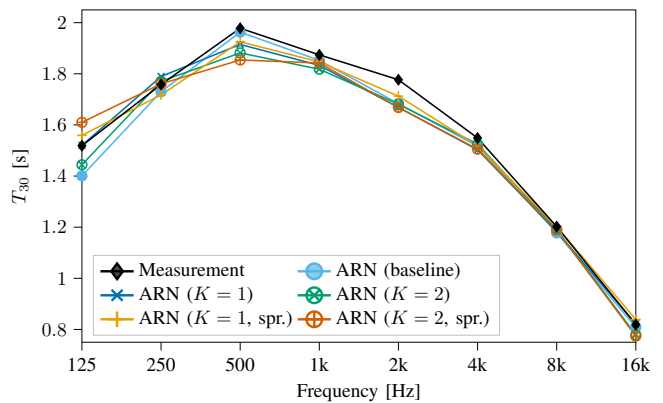


Fig. 14. Octave-band T_{30} comparison against the real measurement in scene CR2, configuration LS1-MP2 [38]. All ARNs except the baseline use a Sinkhorn-Knopp matrix design. The matrix size for all ARNs is $M = 4108$, corresponding to $N = 82$ patches.

results presented here are related to the pair LS1-MP2, but the reported observations apply to all configurations.

The loudspeakers’ and microphones’ directional transfer functions were not applied. As a result, the simulated responses’ normalization might be lacking a scaling factor, but this is inconsequential to all considered metrics (i.e. T_{30} , EDT, NED).

As with the GA comparisons, the method was tested with different matrix and injector designs, injection orders, and surface discretization levels. Changing the level of surface discretization had similar effects to those discussed above. For brevity, results are only reported for one discretization setup, featuring $N = 82$ patches and $M = 4108$ delay lines.

1) *Reverberation time*: All reverberation times are in very good accordance with the ground truth, as shown in Fig. 14. Employing different matrix designs seems to have negligible effects on the T_{30} . This is likely due to the room being mostly convex, and featuring uneven but relatively uniform absorption coefficients. The injector order and design also has minimal effect on the reverberation times, which is expected.

2) *Early reverberation*: The measured responses exhibit relatively early mixing times, most likely due to the intricate details of several walls in the room. On one hand, this means that increasing the injection order and design has little effect on the EDT, as shown in Fig. 15. On the other hand, the injector design is quite relevant in terms of echo density (see Fig. 16), since the application of temporal spreading accelerates the mixing.

All ARNs exhibited a small underestimation of the EDT, as can be seen in Fig. 15. This is to be expected, as was discussed in the previous section (refer back to Fig. 11). The same behaviour was observed for all matrix and injector designs.

V. COMPUTATIONAL COMPLEXITY

The computational complexity of this class of models can be separated between a precomputation cost, an interactive update cost, and an audio processing cost. This section explains what the different components amount to, and provides a qualitative

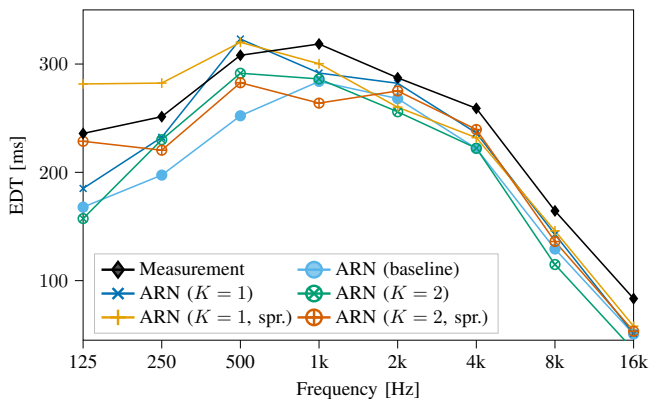


Fig. 15. Octave-band EDT comparison against the real measurement in scene CR2, configuration LS1-MP2 [38]. All ARNs except the baseline use a Sinkhorn-Knopp matrix design. The matrix size for all ARNs is $M = 4108$, corresponding to $N = 82$ patches.

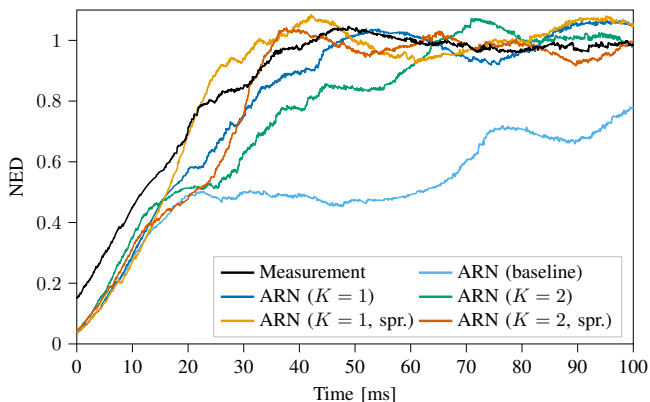


Fig. 16. NED comparison against the real measurement in scene CR2, configuration LS1-MP2 [38]. NED window length 25 ms. All ARNs except the baseline use a Sinkhorn-Knopp matrix design. The matrix size for all ARNs is $M = 4108$, corresponding to $N = 82$ patches.

description of the additional cost associated to the proposed extensions compared to the baseline ARNs [13].

A. Precomputation cost

The precomputation cost includes the calculation of the scattering matrix \mathbf{A} and of the recursion operators d_{ij} . This is the component that is most computationally heavy, as it involves ray-tracing from a high number of surface points. Unless the surface geometry or material properties change over time, these parameters need to be computed only once.

Compared to the baseline ARNs, the matrix designs proposed in this paper also require finding the “closest unlossless” matrix as described earlier. However, the cost of this operation is negligible compared to that of evaluating $\hat{\mathbf{S}}$, which is always required. The recursion operators d_{ij} are unchanged with respect to the baseline.

B. Interactive update cost

The injection, detection, and bypass operators (s_{ij} , r_{ij} , and b , respectively), depend on the positions of sources and

listeners, and therefore need to be recomputed any time they move. More specifically, the injection operators require updating for source movements, the detection operators for receiver movements, and the bypass filter for either. Their computation, as detailed in the previous section, involves $K + 2$ ray-tracing reflections for injectors, and one for detectors.

Compared to the baseline ARNs, the design cost of the injection operators s_{ij} rises linearly with the desired injection order K , due to the additional ray-tracing steps. The detection operators r_{ij} are essentially unchanged with respect to the baseline. If the ISM is employed for the bypass operator b , the associated computational cost rises quadratically (or, in the case of non-rectangular rooms, exponentially) with the desired injection order K . If the RTM is employed instead, there is no additional cost associated to b , since it is evaluated at the same time as s_{ij} (as discussed in the previous section). Note that a hybrid approach can be taken: for example, if the desired injection order is $K = 3$, one could employ ISM for first order reflections, and RTM for second and third order ones.

C. Audio processing cost

The audio processing cost involves running the filter structure as shown in Fig. 2, once all parameters are set. Compared to the baseline ARNs, the additional cost of the proposed extensions comes from the filter operation of the bypass operator b and the injection/detection operators s_{ij} and r_{ij} (if using the temporal spreading method). The feedback matrix \mathbf{A} has the form of a block-matrix for both the baseline ARNs and the proposed extension. However, as opposed to the baseline ARNs, sub-matrices in the proposed extension are no longer Householder matrices. This means that the computational cost for each block increases from $O(M_i)$ to $O(M_i^2)$, where M_i is the size of the block associated to the i^{th} patch.

VI. CONCLUSIONS

This paper was concerned with approximating Acoustic Radiance Transfer (ART), a room acoustic model based on geometrical acoustics (GA), using computationally efficient recursive networks of delay lines called room acoustic rendering networks. Two network designs proposed by Bai *et al.* [13], [14] served as starting point. This paper proposed two key extensions. The first consisted of a physically-informed design of the feedback matrices enabling explicit control of the scattering properties of wall materials. The second involved high-order injection operators enabling to freely scale the number of early reflections modeled accurately and to improve the echo density buildup.

The resulting model was evaluated using objective measures of perceptual features, including frequency-dependent reverberation times, normalized echo density build-up, and early decay times. The evaluation showed that together, the proposed extensions result in a significant improvement over the baseline. This is especially so for rooms with non-convex geometries or unevenly distributed wall absorption, scenarios that are commonly encountered in practical settings and where scattering plays an important role.

The main venues for further improvement of the model are related to the requirements of unilossless matrix design, and to the computational complexity in cases where a high polygon count is required. Future work will involve investigating how to further exploit the structure of ART matrices to reduce approximation errors in the unilossless matrix optimization. Further work will also explore complexity reduction strategies for (a) the operation of the recursive filter component, specifically in the case of real-time rendering of non-convex rooms, which require a fine spatial discretization, and (b) to reduce or remove the need for computationally costly ray-tracing in the precomputation stage, which can be problematic for applications where the room geometry is not known in advance, e.g. AR. Finally, formal listening experiments will be carried out to validate the proposed model perceptually.

ACKNOWLEDGMENTS

We thank Sebastian J. Schlecht for the useful discussions on lossless matrices, and Randall Ali for the useful discussions on notation and presentation of the geometrical aspects.

APPENDIX GEOMETRY TERMS

The definitions presented in this appendix can be found in the literature [21], but since we use different notation and nomenclature, we report them here for clarity. The differential projected area $dA_{p_{x'}}(x)$ and differential solid angle $d\omega_x(x')$, which appear in Eq. (1), are defined as:

$$dA_{p_{x'}}(x) = \max(0, n(x) \cdot v(x|x')) dA(x), \quad (16)$$

$$d\omega_x(x') = \frac{\max(0, n(x') \cdot v(x'|x))}{\|x - x'\|^2} dA(x'), \quad (17)$$

where $n(x)$ is the surface normal at point x , and $\|x - x'\|$ is the distance between x and x' . Note that $n(x') \cdot v(x'|x)$ is the cosine of the angle of incidence from x onto $dA(x')$, and that applying $\max(0, \cos)$ means setting the cosine value to 0 if the direction $v(x'|x)$ is on the “back side” of $dA(x')$.

The following definitions are for the terms which appear in Eq. (3), making up the reflection kernel $R(x, x', v(x'|x''))$. The term ρ is the so-called bidirectional reflectance distribution function (BRDF), defined as

$$\rho(x'|v(x'|x), v(x'|x'')) = \frac{1}{(n(x') \cdot v(x'|x)) L_{\text{in}}(x', v(x'|x))} \times \frac{\partial L_{\text{out}}(x', v(x'|x''))}{\partial \omega_{x'}(x)}. \quad (18)$$

The term G is defined as

$$G(x, x') = \frac{\max(0, n(x) \cdot v(x|x')) \max(0, n(x') \cdot v(x'|x))}{\|x - x'\|^2}. \quad (19)$$

Note how $G(x, x') = G(x', x)$, and

$$G(x, x') dA(x) dA(x') = dA_{p_{x'}}(x) d\omega_x(x') \quad (20)$$

$$= dA_{p_x}(x') d\omega_{x'}(x). \quad (21)$$

The term $V(x, x')$ is a visibility operator, equal to 1 if there is an unobstructed line of sight between the points x and x'

and 0 otherwise. The term $D(x, x')$ is a delay operator, which may also include energy absorption due to propagation.

In the case of a point source located in x_s , the primary reflected radiance is

$$L_0(x, v(x|x'), t) = \rho(x|v(x|x_s), v(x|x')) V(x_s, x) \times D(x_s, x) \Delta_s(x) \frac{P_s(t)}{4\pi} \frac{d\omega_{x_s}(x)}{dA(x)}, \quad (22)$$

where $P_s(t)$ is the source power, and $\Delta_s(x)$ is the source’s transfer function (e.g. loudspeaker’s polar pattern) towards x .

The sound intensity detected by a point receiver located in x_r is defined by the sum $I(x_r, t) = I_D(x_r, t) + I_L(x_r, t)$ of the direct-incidence component $I_D(x_r, t)$ and the reflected component $I_L(x_r, t)$, defined as

$$I_D(x_r, t) = \Delta_r(x_s) V(x_s, x_r) D(x_s, x_r) \frac{\Delta_s(x_r) P_s(t)}{4\pi \|x_r - x_s\|^2}, \quad (23)$$

$$I_L(x_r, t) = \iint_A \Delta_r(x) V(x, x_r) D(x, x_r) \times L(x, v(x|x_r), t) d\omega_{x_r}(x), \quad (24)$$

where $\Delta_r(x)$ is the receiver’s transfer function (e.g. a microphone polar pattern, or HRTF) towards x .

REFERENCES

- [1] J. G. Apostolopoulos, P. A. Chou, B. Culbertson, T. Kalker, M. D. Trott, and S. Wee, “The road to immersive communication,” *Proc. of the IEEE*, vol. 100, no. 4, pp. 974–990, 2012.
- [2] T. Potter, Z. Cvetković, and E. De Sena, “On the relative importance of visual and spatial audio rendering on VR immersion,” *Frontiers in Signal Processing*, vol. 2, 2022.
- [3] M. Geronazzo, J. Y. Tissieres, and S. Serafin, “A minimal personalization of dynamic binaural synthesis with mixed structural modeling and scattering delay networks,” in *Proc. 2020 IEEE Int. Conf. on Acoust., Speech and Sig. Proc. (ICASSP)*, 2020.
- [4] V. Välimäki, J. D. Parker, L. Savioja, J. O. Smith, and J. S. Abel, “Fifty years of artificial reverberation,” *IEEE Trans. on Audio, Speech, and Lang. Proc.*, vol. 20, no. 5, pp. 1421–1448, 2012.
- [5] Alex Southern, Samuel Siltanen, Damian T Murphy, and Lauri Savioja, “Room impulse response synthesis and validation using a hybrid acoustic model,” *IEEE/ACM Trans. on Audio, Speech, and Lang. Proc.*, vol. 21, no. 9, pp. 1940–1952, 2013.
- [6] F. Brinkmann, L. Aspöck, D. Ackermann, S. Lepa, M. Vorländer, and S. Weinzierl, “A round robin on room acoustical simulation and auralization,” *J. Acoust. Soc. Am.*, vol. 145, no. 4, pp. 2746–2760, 2019.
- [7] V. Välimäki, J. Parker, L. Savioja, J. O. Smith, and J. Abel, “More than 50 years of artificial reverberation,” in *Proc. 60th Int. Conf. of the Audio Eng. Soc.*, 2016.
- [8] Michael Vorländer, *Auralization: Fundamentals of Acoustics, Modelling, Simulation, Algorithms and Acoustic Virtual Reality*, Springer, 2008.
- [9] M. R. Schroeder and B. F. Logan, “Colorless artificial reverberation,” *IRE Trans. on Audio*, , no. 6, pp. 209–214, 1961.
- [10] M. R. Schroeder, “Natural sounding artificial reverberation,” *J. Audio Eng. Soc.*, vol. 10, no. 3, pp. 219–223, 1961.
- [11] J. Jot and A. Chaigne, “Digital delay networks for designing artificial reverberators,” presented at the 90th Conv. of the Audio Eng. Soc., 1991.
- [12] D. Rocchesso and J. O. Smith, “Circulant and elliptic feedback delay networks for artificial reverberation,” *IEEE Trans. on Speech and Audio Proc.*, vol. 5, no. 1, pp. 51–63, 1997.
- [13] H. Bai, G. Richard, and L. Daudet, “Geometric-based reverberator using acoustic rendering networks,” in *Proc. 2015 IEEE Workshop on Appl. of Signal Process. to Audio and Acoust. (WASPAA)*, 2015.
- [14] H. Bai, G. Richard, and L. Daudet, “Late reverberation synthesis: From radiance transfer to feedback delay networks,” *IEEE Trans. on Audio, Speech, and Lang. Proc.*, vol. 23, no. 12, pp. 2260–2271, 2015.

- [15] E. De Sena, H. Hacıhabiboğlu, Z. Cvetković, and J. O. Smith, "Efficient synthesis of room acoustics via scattering delay networks," *IEEE/ACM Trans. on Audio, Speech, and Lang. Proc.*, vol. 23, no. 9, pp. 1478–1492, 2015.
- [16] O. Das, S. J. Schlecht, and E. De Sena, "Grouped feedback delay networks with frequency-dependent coupling," *IEEE/ACM Trans. on Audio, Speech, and Lang. Proc.*, vol. 31, pp. 2004 – 2015, 2023.
- [17] T. B. Atalay, Z. S. Gül, E. De Sena, Z. Cvetković, and H. Hacıhabiboğlu, "Scattering delay network simulator of coupled volume acoustics," *IEEE/ACM Trans. on Audio, Speech, and Lang. Proc.*, vol. 30, pp. 582–593, 2022.
- [18] J. Huopaniemi, L. Savioja, and T. Takala, "DIVA virtual audio reality system," in *Proc. 1996 Int. Conf. Auditory Display (ICAD)*, 1996.
- [19] D. Schröder, F. Wefers, S. Pelzer, D. Rausch, M. Vorländer, and T. Kuhlen, "Virtual reality system at RWTH Aachen university," in *Proc. 2010 Int. Symp. room acoustics (ISRA)*, 2010.
- [20] J. M. Palmer and B. G. Grant, *Art of Radiometry*, Berlin: SPIE, 2010.
- [21] S. Siltanen, T. Lokki, S. Kiminki, and L. Savioja, "The room acoustic rendering equation," *J. Acoust. Soc. Am.*, vol. 122, no. 3, pp. 1624–1635, 2007.
- [22] S. Siltanen, T. Lokki, and L. Savioja, "Efficient acoustic radiance transfer method with time-dependent reflections," in *Proc. 2011 Meetings on Acoustics*, 2011, vol. 12.
- [23] W. Binek, A. Pilch, and T. Kamisiński, "Direct application of the difusers' reflection patterns in geometrical acoustics simulations," *Applied Acoustics*, vol. 198, 2022.
- [24] S. J. Schlecht and E. Habets, "On lossless feedback delay networks," *IEEE Trans. on Sig. Proc.*, vol. 65, no. 6, pp. 1554–1564, 2016.
- [25] S. J. Schlecht and E. Habets, "Sign-agnostic matrix design for spatial artificial reverberation with feedback delay networks," in *Proc. 2018 Int. Conf. of the Audio Eng. Soc. on Spatial Reproduction*, 2018.
- [26] R. Sinkhorn and P. Knopp, "Concerning nonnegative matrices and doubly stochastic matrices," *Pacific J. of Math.*, vol. 21, no. 2, pp. 343–348, 1967.
- [27] P. A. Knight, "The sinkhorn–knopp algorithm: convergence and applications," *SIAM J. on Matrix Anal. and Appl.*, vol. 30, no. 1, pp. 261–275, 2008.
- [28] M. Scerbo, O. Das, P. Friend, and E. De Sena, "Higher-order scattering delay networks for artificial reverberation," in *Proc. 2022 Int. Conf. on Digital Audio Effects (DAFx)*, 2022.
- [29] L. Vinesclas, M. Scerbo, H. Hacıhabiboğlu, Z. Cvetković, and E. De Sena, "Low-complexity higher order scattering delay networks," in *Proc. 2023 IEEE Workshop on Appl. of Signal Process. to Audio and Acoust. (WASPAA)*. IEEE, 2023, pp. 1–5.
- [30] K. H. Kuttruff, "Auralization of impulse responses modeled on the basis of ray-tracing results," *J. of the Audio Eng. Soc.*, vol. 41, no. 11, pp. 876–880, 1993.
- [31] H. Kuttruff, *Room acoustics*, Taylor & Francis Group, 2016.
- [32] J. S. Abel and P. Huang, "A simple, robust measure of reverberation echo density," presented at the 121st Conv. of the Audio Eng. Soc., 2006.
- [33] B. Dalenbäck, "Acoustic / the fireverb suite / reflphinder / gratisvolver pro," CATT, 05-Jul-2011. [Online] <https://www.catt.se/>, Accessed: 15-Mar-2022.
- [34] R. Scheibler, E. Bezzam, and I. Dokmanić, "Pyroomacoustics: A python package for audio room simulation and array processing algorithms," in *Proc. 2018 IEEE Int. Conf. on Acoust., Speech and Sig. Proc. (ICASSP)*, 2018.
- [35] "SCReAM IEEE audio samples," [Online] <https://github.com/SCReAM-Surrey/IEEE2024-RIRs>, Accessed: 29-Sep-2023.
- [36] F. Stevens, D. T. Murphy, L. Savioja, and V. Välimäki, "Modeling sparsely reflecting outdoor acoustic scenes using the waveguide web," *IEEE/ACM Trans. on Audio, Speech, and Lang. Proc.*, vol. 25, no. 8, pp. 1566–1578, 2017.
- [37] H. Hacıhabiboğlu, E. De Sena, and Z. Cvetkovic, "Frequency-domain scattering delay networks for simulating room acoustics in virtual environments," in *Proc. 7th IEEE Int. Conf. on Signal Image Tech. & Internet-Based Sys.*, 2011.
- [38] L. Aspöck, M. Vorländer, F. Brinkmann, D. Ackermann, and S. Weinzierl, "Benchmark for room acoustical simulation (BRAS)," *DOI*, vol. 10, pp. 14279, 2020.



virtual reality.



Engineers (IEEE), and a life member of the Acoustical Society of Finland.



ven, Belgium. He held visiting Researcher positions at Stanford University, Stanford, CA, USA, Aalborg University, Aalborg, Denmark, Imperial College London, London, U.K., and King's College London, London, U.K. His research interests include room acoustics modelling, sound field reproduction, beamforming, and binaural modeling. He is a Member of the IEEE Audio and Acoustic Signal Processing Technical Committee, and an Associate Editor for the EURASIP Journal on Audio, Speech, and Music Processing and IEEE/ACM TRANSACTIONS ON AUDIO SPEECH AND LANGUAGE PROCESSING. He was the recipient of an EPSRC New Investigator Award and co-recipient of Best Paper Awards at WASPAA-21 and AVAR-22. For more information see: desena.org.

Matteo Scerbo Matteo Scerbo received his Bachelor's degree in computer engineering from the Università di Genova (UniGe) in 2017. He then specialized in acoustics and audio signal processing, receiving his Master's degree in Music and Acoustics Engineering at the Politecnico di Milano (PoliMi) in 2021. Since 2021, he has been a PhD student in Audio Engineering at the University of Surrey (UoS), investigating efficient methods for room acoustics modeling. His interests include room acoustics modeling, digital signal processing, and

Lauri Savioja Lauri Savioja (M'00-SM'08) works as a professor at the Department of Computer Science at Aalto University, Finland. He received his doctorate from the Helsinki University of Technology in 1999 majoring in computer science while his thesis topic was room acoustic modeling. His research interests include room acoustics, virtual reality, and parallel computation. Prof. Savioja is a fellow of the Audio Engineering Society (AES) and of the Acoustical Society of America (ASA), senior member of the Institute of Electrical and Electronics Engineers (IEEE), and a life member of the Acoustical Society of Finland.

Enzo De Sena Enzo De Sena (Senior Member, IEEE) received the M.Sc. degree (cum laude) in telecommunication engineering from the Università di Napoli "Federico II," Naples, Italy, in 2009, and the Ph.D. degree in electronic engineering from King's College London, London, U.K., in 2013. He is currently an Associate Professor (Reader) at the University of Surrey, Guildford, U.K., where he serves as Director of the Institute of Sound Recording (IoSR). Between 2013 and 2016, he was a Postdoctoral Researcher with KU Leuven, Leu-